

Collisionless Relaxation of a Disequibrated Current Sheet and Implications for Bifurcated Structures

Young Dae Yoon (✉ yoon11@postech.ac.kr)

Pohang Accelerator Laboratory <https://orcid.org/0000-0001-8394-2076>

Gunsu Yun

Pohang University of Science and Technology (POSTECH) <https://orcid.org/0000-0002-1880-5865>

James Burch

Southwest Research Institute <https://orcid.org/0000-0003-0452-8403>

Deirdre Wendel

NASA Goddard Space Flight Center <https://orcid.org/0000-0002-1925-9413>

Article

Keywords: Magnetic Phenomena, Phase-space Distributions, Single-particle Orbit Classes, Particle-in-cell Simulations, Bifurcated Current Sheets

Posted Date: March 25th, 2021

DOI: <https://doi.org/10.21203/rs.3.rs-343769/v1>

License:  This work is licensed under a Creative Commons Attribution 4.0 International License.

[Read Full License](#)

Version of Record: A version of this preprint was published at Nature Communications on June 18th, 2021. See the published version at <https://doi.org/10.1038/s41467-021-24006-x>.

1 **Collisionless Relaxation of a Disequibrated Current Sheet and**
2 **Implications for Bifurcated Structures**

3 Young Dae Yoon*

4 *Pohang Accelerator Laboratory, POSTECH, Pohang, Republic of Korea*

5 Gunsu S. Yun*

6 *Department of Physics, POSTECH, Pohang, Republic of Korea*

7 Deirdre E. Wendel

8 *NASA Goddard Space Flight Center, Greenbelt, MD, USA*

9 James L. Burch

10 *Southwest Research Institute, San Antonio, TX, USA*

Abstract

Current sheets are ubiquitous plasma structures that play the crucial role of being energy sources for various magnetic phenomena. Although a plethora of current sheet equilibrium solutions have been found, the collisionless process through which a disequibrated current sheet relaxes or equilibrates remains largely unknown. Here we show, through analyses of phase-space distributions of single-particle orbit classes and particle-in-cell simulations, that collisionless transitions among the orbit classes are responsible for this process. Bifurcated current sheets, which are readily observed in geospace but whose origins remain controversial, are shown to naturally arise from the equilibration process and thus are likely to be the underlying structures in various phenomena; comparisons of spacecraft observations to particle-in-cell simulations support this fact. The bearing of this result on previous explanations of bifurcated structures is also discussed.

11 I. INTRODUCTION

12 Current sheets are structures generated by opposing magnetic fields and are ubiquitous
13 in magnetized plasmas such as solar flares[1], the solar wind[2], the heliosphere[3, 4], and
14 planetary magnetospheres[5, 6]. It is also deeply related to magnetic reconnection[7, 8], a
15 process in which the energy stored in magnetic fields is converted to particle kinetic energies.
16 Current sheets have thus been subject to extensive research, and a plethora of equilibrium
17 solutions have been found both analytically[9–16] and numerically[17–20].

18 However, there remains an important outstanding question regarding current sheet equi-
19 libria. Although various equilibrium solutions have been found, the collisionless process
20 through which a disequilibrated current sheet equilibrates remains largely unknown. Such
21 knowledge is crucial because plasmas in general do not start from equilibria, and also because
22 it elucidates how a given system “wants” to evolve in time, even if it does not eventually
23 equilibrate. In addition, the equilibria that have been found are specific solutions; a com-
24 prehensive understanding of the equilibration or relaxation process is necessary in order to
25 place current sheets in a general context.

26 A commonly observed form of current sheets is a bifurcated current sheet, which has
27 two current density peaks on either side of the symmetry plane. These were first observed
28 in the Earth’s magnetotail by Cluster spacecraft measurements[21, 22] and were initially
29 deemed atypical. Later analyses, however, showed that bifurcated current sheets are actually
30 extremely common, and that they were detected $\sim 25\%$ of the time Cluster was in the
31 magnetotail current sheet[23, 24]. Since then, various explanations have been put forth,
32 including flapping motion[25], magnetic reconnection[26, 27], temperature anisotropy[28, 29],
33 Speiser motion[30], and non-adiabatic scattering of particles in a strongly curved magnetic
34 field[16]. However, there is no consensus on the origin of bifurcated current sheets, which
35 largely remains a mystery despite being readily observed even to this day[31–33].

36 In this paper, the collisionless relaxation process of an initially disequilibrated current
37 sheet is studied. The process is shown in three steps. First, particle orbits in a magnetic
38 field reversal are comprehensively categorized into four orbit classes. Second, the phase-
39 space distribution of each orbit class and the role each class plays with respect to current
40 sheet density, temperature, and strength are examined. Finally, with the aid of particle-
41 in-cell simulations, it is shown that transitions among the orbit classes are responsible for

42 collisionless current sheet relaxation. The final equilibrium is most naturally understood in
 43 terms of the relative population of the phase-space distributions of the four orbit classes,
 44 instead of closed-form functions such as a Maxwellian.

45 The bearing of this process on the origin of bifurcated current sheets is then discussed.
 46 Two of the orbit classes necessarily exhibit spatially bifurcated structures, and so such
 47 structures naturally arise as a current sheet evolves towards equilibrium via orbit class
 48 transitions. An exemplary equilibrium from particle-in-cell simulations is compared with
 49 Magnetospheric Multiscale (MMS) measurements of an electron-scale current sheet, and
 50 their profiles are shown to agree well. The relevance of the relaxation process to previous
 51 explanations of bifurcated current sheets is also discussed.

52 II. RESULTS

53 **Particle Orbit Classes** Let us first examine single-particle dynamics in the renowned
 54 Harris current sheet[9], which is chosen as the system of scrutiny in the present study. It is
 55 described by the following magnetic field profile and distribution function f_σ for species σ
 56 (i for ions and e for electrons):

$$\mathbf{B}(x) = \hat{y}B_0 \tanh \frac{x}{\lambda}, \quad (1)$$

$$f_\sigma(x, \mathbf{v}, t) = \left(\frac{1}{2\pi v_{T\sigma}^2} \right)^{3/2} \frac{n_0}{\cosh^2(x/\lambda)} \\ \times \exp \left[-\frac{1}{2v_{T\sigma}^2} (v_x^2 + v_y^2 + (v_z - V_\sigma)^2) \right], \quad (2)$$

57 where B_0 is the asymptotic value of the magnetic field, λ is the sheath thickness, n_0 is the
 58 sheath peak density, and $v_{T\sigma} = \sqrt{k_B T_\sigma / m_\sigma}$ is the species thermal velocity where T_σ and
 59 m_σ are respectively the species temperature and mass. V_σ is the species' mean velocity
 60 in the z -direction, i.e., its drift velocity. It is also assumed that $T_i = T_e := T$ and $V_i =$
 61 $-V_e := V$; the latter can always be made true by choosing a frame of reference where the
 62 electrostatic potential $\phi = 0$. Two conditions must be true in order for this system to be
 63 an exact solution of the stationary Vlasov equation: (i) $B_0 = 2\sqrt{\mu_0 n_0 k_B T}$, which describes
 64 the balance between the peak magnetic pressure $B_0^2/2\mu_0$ and the peak thermal pressure
 65 $n_0 k_B (T_i + T_e) = 2n_0 k_B T$, and (ii) $\lambda = \lambda_D c/V$ where $\lambda_D = \sqrt{\epsilon_0 k_B T / n_0 e^2}$ is the Debye

66 length and c is speed of light, which determines the equilibrium sheath thickness.

67 The vector potential is chosen to be $\mathbf{A} = -\hat{z}\lambda B_0 \ln \cosh x/\lambda$. Normalizing length by
 68 λ , mass by the species mass m_σ , and time by $\omega_{c\sigma} = q_\sigma B_0/m_\sigma$ where q_σ is the species
 69 charge, then a particle obeys Lagrangian dynamics with the normalized Lagrangian $\bar{L} =$
 70 $(\bar{v}_x^2 + \bar{v}_y^2 + \bar{v}_z^2)/2 - \bar{v}_z \ln \cosh \bar{x}$, where barred quantities are normalized to their respective
 71 reference units, i.e., $\bar{L} = L/m_\sigma \lambda^2 \omega_{c\sigma}^2$, $\bar{v}_x = v_x/\lambda \omega_{c\sigma}$, and $\bar{x} = x/\lambda$. Because y and z are
 72 ignorable coordinates, there are three constants of motion, namely the canonical momenta
 73 $\bar{p}_y = \partial \bar{L}/\partial \bar{v}_y = \bar{v}_y$ and $\bar{p}_z = \partial \bar{L}/\partial \bar{v}_z = \bar{v}_z - \ln \cosh \bar{x}$, and the total energy of the parti-
 74 cle (recall that $\phi = 0$), $\bar{H} = (\bar{v}_x^2 + \bar{v}_y^2 + \bar{v}_z^2)/2 = \bar{v}_x^2/2 + [\bar{p}_y^2 + (\bar{p}_z + \ln \cosh \bar{x})^2]/2$. The
 75 normalized effective potential $\chi(\bar{x})$ of the motion in the x -direction is therefore $\chi(\bar{x}) =$
 76 $[\bar{p}_y^2 + (\bar{p}_z + \ln \cosh \bar{x})^2]/2$.

77 Analyzing the extrema of $\chi(\bar{x})$ shows that it exhibits two shapes depending on the sign of
 78 \bar{p}_z : (i) a single-well if $\bar{p}_z > 0$ (e.g., black line in Fig. 1d), and (ii) a double-well with a local hill
 79 at $\bar{x} = 0$ if $\bar{p}_z < 0$ (e.g., black line in Fig. 1a). In case (ii), if a particle does not have enough
 80 energy to overcome the local hill, i.e., $\bar{H} < \chi(0)$ or equivalently $\sqrt{\bar{v}_x^2 + \bar{v}_z^2} = \bar{v}_\perp < -\bar{p}_z$,
 81 it oscillates within one of the two wells and does not cross $\bar{x} = 0$. In the opposite case
 82 where $\bar{v}_\perp > -\bar{p}_z$, the particle has enough energy to overcome the hill and thus undergoes
 83 a full double-well orbit while crossing $\bar{x} = 0$. This double-well orbit class can be further
 84 divided into two sub-classes depending on the particle's bounce-period-averaged velocity in
 85 the z -direction $\langle \bar{v}_z \rangle$. Because $\langle \bar{v}_z \rangle = \langle \bar{p}_z \rangle + \langle \ln \cosh \bar{x} \rangle$ while $\bar{p}_z < 0$ is a constant in the case
 86 of a double-well χ , a particle can have either a positive or negative $\langle \bar{v}_z \rangle$ depending on its
 87 oscillation amplitude in the x -direction; particles with higher energies have higher values of
 88 $\langle \ln \cosh \bar{x} \rangle$ and thus can have positive values of $\langle \bar{v}_z \rangle$.

89 Figure 1 summarizes the four classes of particle orbits. The black lines in Figs. 1a-d show
 90 the effective potential χ of each class, and the three dashed lines in each panel represent the
 91 energies of three particles with differing values of initial \bar{v}_x and thus of \bar{H} . Each particle is
 92 distinguished by its respective color (blue, red, or cyan). The three lines in Figs. 1e-h show
 93 the motion of the three particles in the left panels in the $x - z$ plane, and the black dots
 94 represent their starting positions.

95 Figure 1e represents the non-crossing orbit class[34], hereafter denoted NC, where the
 96 particles are simply ∇B drifting with $\langle \bar{v}_z \rangle < 0$. Figure 1f represents the class where particles
 97 undergo full double-well motion with $\langle \bar{v}_z \rangle < 0$, hereafter denoted DW-. The blue particle in

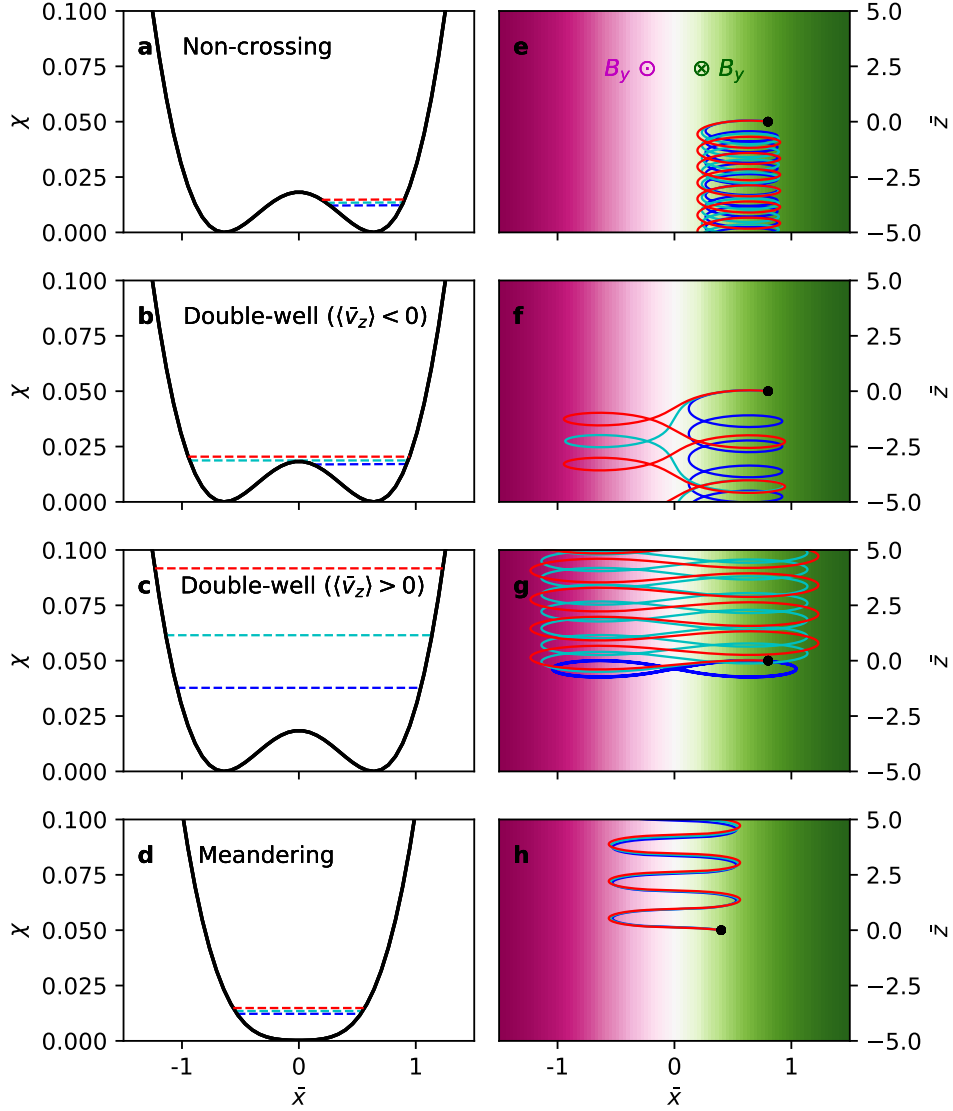


FIG. 1. **Four classes of particle orbits and their effective potentials.** Effective potentials χ of the **a** non-crossing (NC) orbit class, **b** double-well orbit class with a negative time-averaged velocity ($\langle \bar{v}_z \rangle < 0$; DW-), **c** double-well orbit class with a positive time-averaged velocity ($\langle \bar{v}_z \rangle > 0$; DW+), and **d** meandering (M) orbit class. **e-h** Particle orbits in the $\bar{x} - \bar{z}$ plane respectively belong to the four classes in **a-d**. Three particles are plotted for each class and are labelled by the blue, cyan, and red colors. Each particle's energy is represented by its corresponding color in **a-d**. The blue particles in **f** and **g** respectively belong to NC and DW- but are plotted to show the NC \rightarrow DW- and DW- \rightarrow DW+ transitions.

98 Figure 1f belongs to NC but is plotted to show the transition from NC to DW−. Figure 1g
 99 represents the other class where $\langle \bar{v}_z \rangle > 0$, hereafter denoted DW+. Again, the blue particle
 100 belongs to the DW− class but is plotted to show the transition from DW− to DW+. Figure
 101 1h represents the meandering or Speiser orbit class[35] with $\langle \bar{v}_z \rangle > 0$, hereafter denoted M.

102 The DW+ class was previously identified in a context with curved magnetic fields as
 103 “cucumber orbits[36, 37]” due to its cucumber shape. Here we have re-identified the class
 104 to clarify the physical origin of such motion and to distinguish more clearly between DW+
 105 and DW−, the latter of which does not exhibit cucumber shapes.

106 **Phase-Space Distributions** Now let us examine how each orbit class is represented
 107 in phase space. 10^8 particles were randomly sampled from Eq. 2 with $\bar{V}_\sigma = 0.005$ and
 108 $\bar{v}_{T\sigma} = 0.05$ — these specific values satisfy the equilibrium condition for the Harris sheet.
 109 Figure 2 shows the phase space distributions (a-c) and velocity space histograms (d-f) in
 110 each velocity direction, and Fig. 2g shows the spatial histograms. The orbit classes are
 111 distinguished by the black, red, green, and blue colors. The dotted lines and the arrows
 112 in the right panels correspond to the mean velocity and the velocity spread (two standard
 113 deviations) of each orbit class.

114 The phase-space distribution of each orbit class has its own contribution to current sheet
 115 density, temperature, and strength. The spatial distribution in Fig. 2g is related to the
 116 density, and the spreads and means of the velocity distributions in Figs. 2d-f are respectively
 117 related to the temperature and current strength of each orbit class.

118 Figure 2d shows that the velocity spread and hence the temperature in the x -direction,
 119 T_{xx} , has the following hierarchy: NC < DW− < DW+. This is because the transition from
 120 NC to DW necessarily involves a passage through the unstable equilibrium as in Fig. 1b,
 121 which in turn involves a breakdown of adiabatic invariance and phase-mixing[38]. T_{xx} of the
 122 M class is equal to the overall equilibrium temperature. The mean velocity in the x -direction
 123 is befittingly zero for all classes due to symmetry.

124 Figure 2e shows that all classes have the same temperatures and zero mean velocities in
 125 the y -direction, since \bar{v}_y is a constant of motion.

126 Figure 2f shows that the temperature in the z -direction has the hierarchy M < DW+ <
 127 NC < DW−. The NC and DW− classes have negative mean velocities and the other two
 128 have positive mean velocities.

129 Figure 2g shows that the three non-NC classes are spatially concentrated near the center.

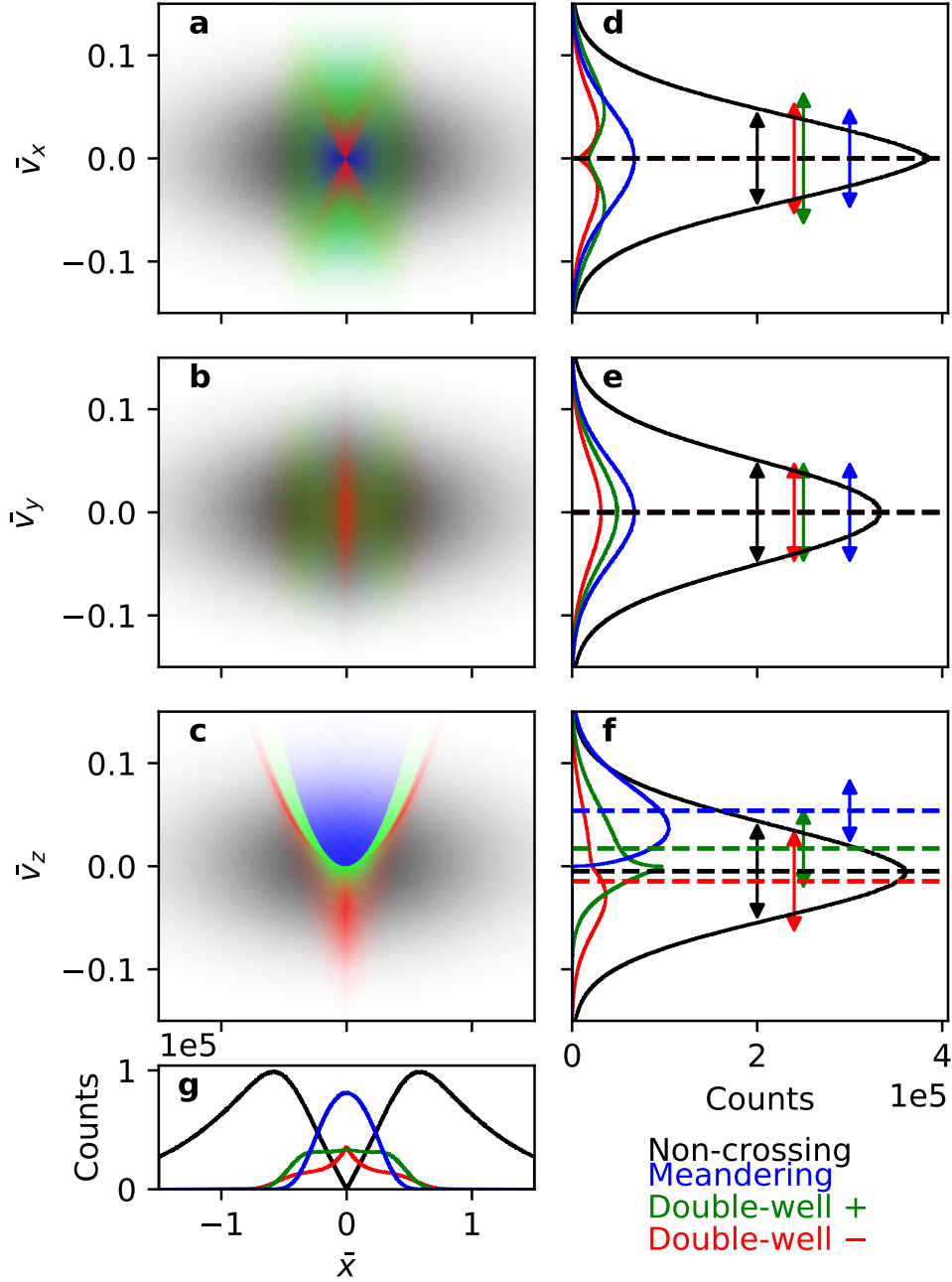


FIG. 2. **Particle distribution in phase space, velocity space, and physical space.** Phase space distributions of the four orbit classes distinguished by the blue, green, red, and black colors in **a** $\bar{x} - \bar{v}_x$ space, **b** $\bar{x} - \bar{v}_y$ space, and **c** $\bar{x} - \bar{v}_z$ space. Particle histograms in **d** \bar{v}_x , **e** \bar{v}_y , and **f** \bar{v}_z . The dotted lines and arrows are respectively the average velocities and two standard deviations of each distribution. **g** Particle histogram in \bar{x} .

130 Also, the DW classes have relatively flat-top density profiles compared to the M class, a
 131 trait which will be revisited later.

132 **Equilibration Process** We now have all the ingredients to understand how an initially
 133 disequilibrated current sheet equilibrates. Let us consider an under-heated Harris current
 134 sheet with a temperature lower than its equilibrium value. In this case, because the thermal
 135 pressure at the center is lower than the magnetic pressure at the outskirts, one expects
 136 heating and pinching (increase of current density) of the current sheet that lead to a new
 137 equilibrium.

138 Let us first predict how the heating and pinching will happen. Inserting Eqs. 1 and 2 in
 139 the Vlasov equation yields

$$\frac{\partial \ln f_\sigma}{\partial \bar{t}} = -2 \left(\frac{\bar{V}_\sigma}{2\bar{v}_{T\sigma}^2} - 1 \right) \bar{v}_x \tanh \bar{x}. \quad (3)$$

140 At equilibrium, the Harris sheet has $\bar{V}_\sigma = 2\bar{v}_{T\sigma}^2$, which can be confirmed by matching the
 141 current density obtained by $\mathbf{J} = \nabla \times \mathbf{B}/\mu_0$ and that obtained by $\mathbf{J} = \sum_\sigma q_\sigma \int \mathbf{v} f_\sigma d^3\mathbf{v}$.
 142 However, if the sheet is under-heated so that $2\bar{v}_{T\sigma}^2 < \bar{V}_\sigma$, then the quantity $\xi := \bar{V}_\sigma - 2\bar{v}_{T\sigma}^2$
 143 is positive and Eq. 3 yields a solution linear in a small time interval $\Delta\bar{t}$:

$$f_\sigma \propto \exp \left[-\frac{1}{2\bar{v}_{T\sigma}^2} (\bar{v}_x + \xi \Delta\bar{t} \tanh \bar{x})^2 \right]. \quad (4)$$

144 The mean velocity in the x -direction is thus $\bar{V}_x(\bar{x}) = -\xi \Delta\bar{t} \tanh \bar{x}$. At positive \bar{x} , particles
 145 gain negative \bar{v}_x and vice-versa; therefore, the initial linear response of an under-heated
 146 Harris sheet is to bring particles closer to the center by increasing their $|\bar{v}_x|$.

147 This response induces transitions among particle classes. It is apparent from Fig. 1a-c
 148 that an increase in $|\bar{v}_x|$ moves NC particles to DW- and DW- particles to DW+. Applying
 149 the analysis of the phase-space distributions of the four classes in Fig. 2, these class tran-
 150 sitions explain (i) current sheet heating in the x -direction, and (ii) current sheet pinching
 151 due to increases in both density and mean velocity at the center (note that the velocity
 152 decrease from the NC \rightarrow DW- transition is more than compensated for in the DW- \rightarrow
 153 DW+ transition). Also, there is no transition to or from the M class because the shape of
 154 χ is such that a change in \bar{v}_x does not induce orbit class transitions.

155 The above analysis only considers linear dynamics assuming that the current sheet profile
 156 remains stationary. It is therefore not valid in the nonlinear regime where the profile self-
 157 consistently changes along with orbit class transitions. However, we may infer from the

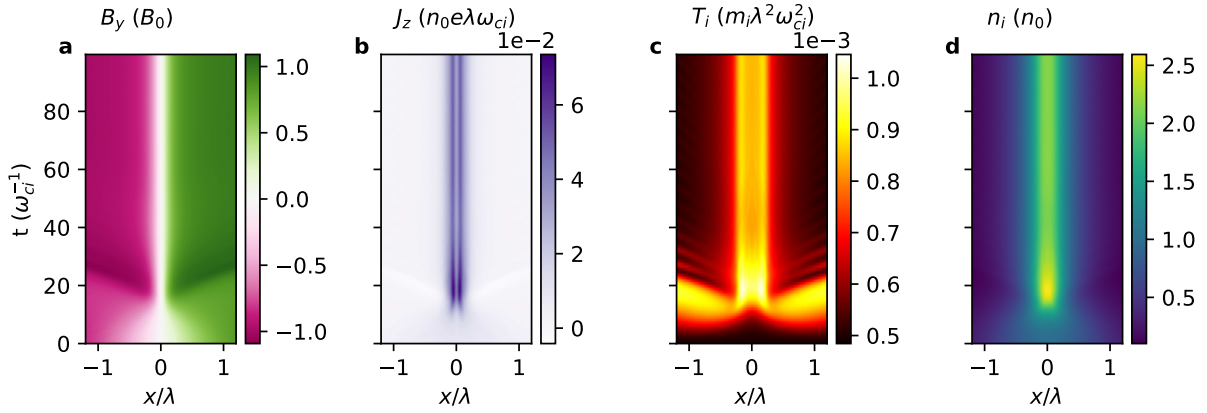


FIG. 3. **Streak plots of variables from the particle-in-cell simulation.** Streak plots of **a** the sheared magnetic field B_y , **b** the current density J_z , **c** the ion temperature T_i , and **d** the ion density n_i from $t = 0$ to $1000\omega_{ci}^{-1}$.

158 analysis the primary mechanism—at least in the linear regime—underlying current sheet
 159 heating and pinching: transitions from the NC class to the DW classes and no transitions
 160 to or from the M class.

161 These predictions will now be verified with a one-dimensional particle-in-cell simulation.
 162 The initial condition was an under-heated Harris current sheet with a temperature $T =$
 163 $0.2T_{\text{eq}}$ where $T_{\text{eq}} = B_0^2 / (4\mu_0 n_0 k_B)$ is the Harris equilibrium temperature. The initial sheet
 164 thickness was $\lambda = 10d_i$ where d_i is the collisionless ion skin depth. Figure 3 shows streak
 165 plots of B_y , J_z , the ion temperature T_i , and the ion density n_i . The current sheet pinches
 166 and heats up until $\sim 30\omega_{ci}^{-1}$, after which it remains steady and thus reaches equilibrium.

167 Figures 4a-c show f_i in $x - v_x$ space at $t = 0, 10, 100\omega_{ci}^{-1}$, respectively. Figure 4b confirms
 168 the initial response of the under-heated current sheet as predicted by Eq. 4, namely the
 169 focussing of the particles towards the center. Figure 4c shows the equilibrium reached by
 170 f_i , and Fig. 4d shows the difference (Δf_i) between the initial state (Fig. 4a) and the
 171 equilibrium state (Fig. 4c). Comparing Fig. 4d to Fig. 2a, it is apparent that the NC
 172 class de-populates and migrates to the DW classes. The dynamics in the simulation is fully
 173 nonlinear, so transition to the M class also occurs, albeit less significantly than the main
 174 NC \rightarrow DW transition.

175 Figures 4e-g and 4i are the same as Figs. 4a-d except that they are in $x - v_z$ space.
 176 Again, the NC \rightarrow DW transition is evident from a comparison to the pronounced Y-shape

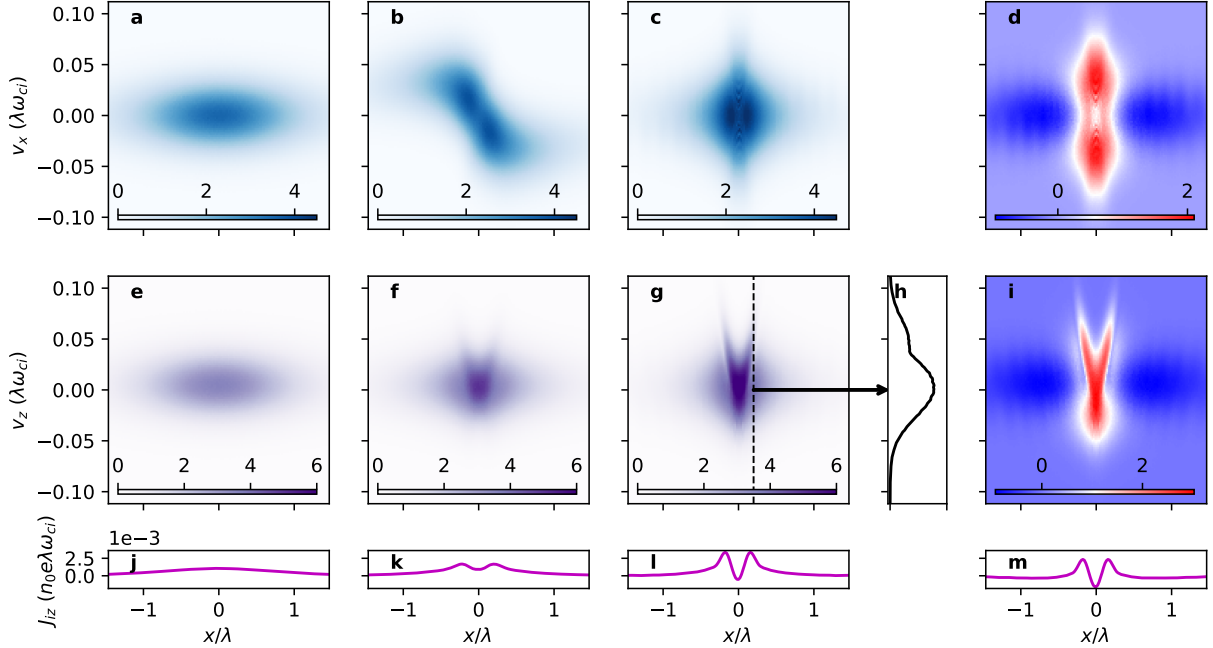


FIG. 4. **Time evolution of the ion distribution function from the particle-in-cell simulation.** Ion distribution function f_i in $x-v_x$ space at **a** $t = 0$, **b** $t = 10\omega_{ci}^{-1}$, and **c** $t = 100\omega_{ci}^{-1}$. **d** The difference (Δf_i) between f_i in **c** and **a**. **e-g** and **i** are respectively the same as **a-c** and **d**, except in $x-v_z$ space. **h** A slice through the dotted line in **g**. **j-l** The ion current density J_{iz} obtained by taking the first velocity moment of **e-g**. **m** The difference between **j** and **l**.

177 of the phase-space distribution of the DW classes (Fig. 2c). Therefore, we have confirmed
 178 that collisionless equilibration of an under-heated Harris current sheet is mainly due to orbit
 179 class transitions from NC to DW.

180 It is clear from Figs. 4c and 4g that the final equilibrium is most naturally described by the
 181 relative population in each orbit class, rather than, e.g., Maxwellian or kappa distributions.
 182 Figure 4h shows the distribution in v_z at $x = 0.2\lambda$, whose profile is clearly non-Maxwellian.

183 Note that electrons also mainly transition from NC to DW in this process because the
 184 orbit classes apply generally for any species. Figure 4 is therefore qualitatively applicable
 185 to electrons, except that their velocities change signs due to their negative charge.

186 **Origin of Bifurcated Current Sheets** Figures 4j-l show the time evolution of the
 187 ion current density in the z -direction, J_{iz} , and Fig. 4m shows the difference between the
 188 initial and final J_{iz} . The bifurcated structure is evident, which naturally arises from the
 189 pronounced Y-shape of the phase-space distribution of the DW classes to which particles

190 migrate from the NC class. The total current density—mainly carried by the electrons—
 191 is also bifurcated, as shown in Fig. 3b. Bifurcated current structures are thus natural
 192 by-products of the collisionless equilibration process of a current sheet.

193 Let us compare the simulation results with a current sheet detected by the Magnetospheric
 194 Multiscale (MMS) mission[39] from 20:24:00 to 20:24:15 UT on 17 June 2017, when the space-
 195 craft was located at $(-19.4, -10.4, 5.5) R_e$ in Geocentric Solar Ecliptic (GSE) coordinates
 196 while crossing the magnetotail plasma sheet from the southern to the northern hemisphere.
 197 This sheet has also been examined in previous studies under different contexts[33, 40, 41].
 198 The focus will now be on electrons instead of ions because the observed current sheet has
 199 an electron scale thickness ($< 10d_e$), and as a confirmation that electrons have similar orbit
 200 class transition dynamics to that of ions.

201 Figure 5 shows a side-by-side comparison of the current sheet detected by MMS and that
 202 from the particle-in-cell simulations. The data are presented using a local coordinate system,
 203 LMN . The sheared magnetic field is in the L -direction, and M and N are respectively
 204 parallel and normal to the current sheet. The current is carried mainly by the electrons in
 205 both the observation and the simulation. The finite electron outflow v_{eL} in Fig. 5b indicates
 206 that the observed current sheet is undergoing magnetic reconnection, whereas the simulated
 207 current sheet, being one-dimensional, is not. Reconnection induces perpendicular electron
 208 heating at the sheet center[42], which explains the central increase of T_{eMM} in Fig. 5d
 209 relative to Fig. 5j. The relative increase of T_{eLL} at the outskirts in Fig. 5d is also attributed
 210 to reconnection-induced parallel electron heating[42].

211 Apart from such reconnection-related dissimilarities, the observed and simulated profiles
 212 agree strikingly well, including the bifurcated current structure. In particular, the simulated
 213 equilibrium explains the central dip and increased outskirts of the electron temperature
 214 tensor element T_{eMM} relative to T_{eNN} , as shown in Figs. 5d and 5j. The profile of $T_{eNN} -$
 215 T_{eMM} in Fig. 5e is remarkably reproduced by Fig. 5k, except for the relative central dip
 216 in Fig. 5e due to the reconnection-induced increase of T_{eMM} . Same goes for the pressure
 217 tensor elements P_{eMM} , P_{eNN} , and $P_{eNN} - P_{eMM}$ (Figs. 5f and 5l).

218 The increased amount of electron population in the DW classes is shown not only by the
 219 current, temperature, and pressure structures, but also by the density plateau in Fig. 5c
 220 and 5i which is due to migrations to the DW classes (see Fig. 2g). This density plateau was
 221 also observed in Cluster measurements[25].

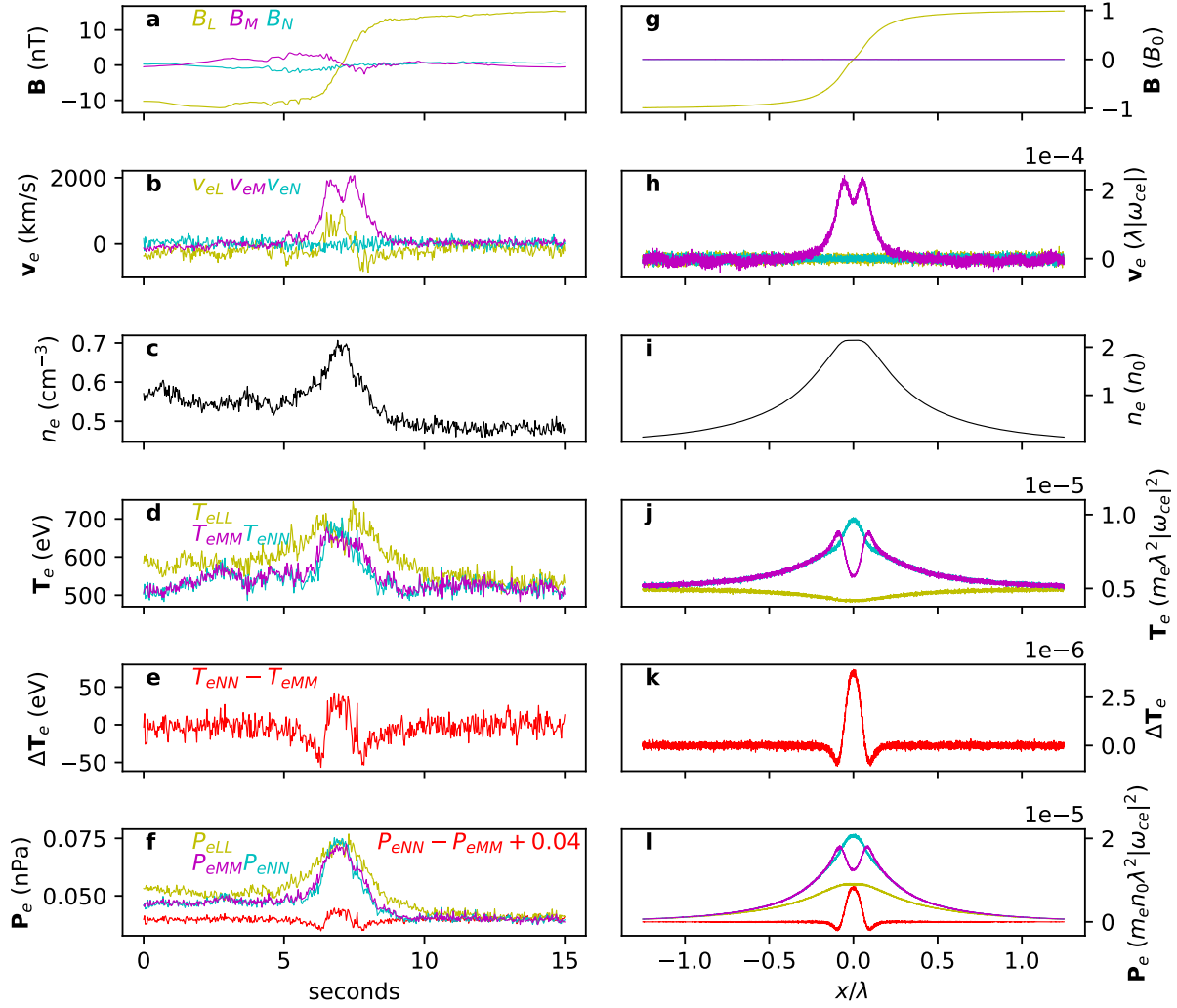


FIG. 5. Comparison of a current sheet detected by MMS to that from the particle-in-cell simulation. **a-f** Sequentially, the magnetic field \mathbf{B} , electron velocity \mathbf{v}_e , electron density n_e , diagonal elements of the electron temperature tensor \mathbf{T}_e , the difference between the temperature tensor elements $T_{eNN} - T_{eMM}$, and diagonal elements of the electron pressure tensor \mathbf{P}_e and $P_{eNN} - P_{eMM}$ (shifted up by 0.04) detected by the Magnetospheric Multiscale spacecraft from 20:24:00 to 20:24:15 UT on 17 June 2017. The x -axis is seconds from 20:24:00 UT. **g-l** Quantities from the particle-in-cell simulation respectively corresponding to **a-f**.

222 III. DISCUSSION

223 Although the new kinetic equilibrium has been presented as an example of bifurcated
 224 current sheets, we are not claiming that all such sheets are in equilibrium states. Instead,

225 the claim is that bifurcated structures are natural repercussions of the collisionless current
226 sheet equilibration process and so are likely to be observed in a variety of phenomena as
227 the underlying structure. As mentioned in the Introduction, numerous explanations for
228 bifurcated current sheets have been put forth; these explanations will now be unravelled in
229 relation to the relaxation process.

230 Magnetic reconnection has been one of the proposed causes of bifurcated current sheets[26,
231 43], but many such sheets were also observed without any fast flows[25, 44] which are sig-
232 natures of reconnection. Nevertheless, a statistical study indicated that the thinner the
233 structures are, the more likely they are to be bifurcated[24]. These observations can be
234 unified by the fact that thinner current sheets are more likely to involve sub-skin-depth
235 collisionless dynamics, which is favorable for the occurrence of both collisionless recon-
236 tion and the present collisionless relaxation process. A possible scenario is one where an
237 initially thick, under-heated current sheet equilibrates to a thin, sub-skin-depth bifurcated
238 structure, which then undergoes collisionless reconnection. In fact, the initial condition for
239 reconnection in collisionless situations is more likely to be the equilibrium presented here
240 than widely-used specific solutions such as the Harris sheet[45]. If the sheet does not thin
241 enough for reconnection to occur, then it may remain bifurcated and steady.

242 Flapping motion was also observed in conjunction with bifurcated current sheets[25,
243 27]. This motion involves fast thinning and thickening of the sheet[27]. Such fast motion
244 will naturally induce bifurcation via two possible scenarios: (i) disequilibrium of current
245 sheets, followed by relaxation via spontaneous orbit classes transitions, or (ii) unspontaneous
246 transitions driven by the external source that thins the sheet.

247 Equilibria involving anisotropic temperatures have also been shown to exhibit bifurcated
248 structures[13, 28, 29], but the source of the anisotropy was not clear so the amount of
249 anisotropy had been set *ad-hoc*. The present collisionless relaxation process naturally induces
250 temperature anisotropy, which is thus an innate result of the equilibration process rather
251 than a cause of bifurcated structures.

252 Speiser motion (M class) was also attributed to bifurcated structures[17, 30]. However,
253 it is clear from Fig. 2 that the M class cannot contribute to bifurcated structures if the
254 density is peaked near the center, unless the density itself is bifurcated[17] and/or heavier
255 species are taken into account[30].

256 Some studies[16, 36, 37] invoke non-adiabatic scattering of particles from M to DW+ via

257 a slow diffusive process in current sheet equilibria. However, the diffusion coefficient of such
 258 process is zero for $B_x = 0$ because it scales with the curvature parameter κ (cf. equation 7
 259 of Zelenyi et al.[37]). We have shown here that neither curved magnetic fields nor diffusive
 260 processes are necessary; simply choosing a disequilibrated initial state is sufficient for the
 261 development of bifurcated structures, although diffusion due to field curvature may aid the
 262 process.

263 In summary, the collisionless relaxation process of a disequilibrated current sheet was
 264 studied. The process is most naturally understood by orbit class transitions, which were
 265 analytically predicted and numerically verified. The relaxation mechanism was identified as
 266 the origin of bifurcated current sheets, and the significance of this identification in regards
 267 to previous explanations of bifurcated structures was discussed.

268 IV. METHODS

269 **Sampling from and categorization of the Harris distribution function** Particle
 270 positions and velocities were sampled from Eq. 2 using the `numpy.random` package in Python
 271 3.8. Particles with $\bar{p}_z > 0$ and $\bar{p}_z < -\bar{v}_\perp$ were categorized into M and NC, respectively. For
 272 the rest of the particles that belong to the DW classes, the following steps were taken to
 273 further categorize them.

274 First, a simple analysis of the Hamiltonian of each particle shows that its oscillation
 275 amplitude in the x -direction is given by $\bar{x}_{\max} = \operatorname{arccosh}(\exp[\bar{v}_\perp - \bar{p}_z])$. The bounce-period-
 276 averaged \bar{v}_z of the particle is then given by

$$\langle \bar{v}_z \rangle = \frac{2}{T_0} \int_{-\bar{x}_{\max}}^{\bar{x}_{\max}} \frac{\bar{v}_z}{\bar{v}_x} d\bar{x}, \quad (5)$$

$$= \frac{2}{T_0} \int_{-\bar{x}_{\max}}^{\bar{x}_{\max}} \frac{\bar{p}_z + \ln \cosh \bar{x}}{\sqrt{(\bar{p}_z + \ln \cosh \bar{x}_{\max})^2 - (\bar{p}_z + \ln \cosh \bar{x})^2}} d\bar{x}, \quad (6)$$

277 where $T_0 = 2 \int_{-\bar{x}_{\max}}^{\bar{x}_{\max}} d\bar{x}/\bar{v}_x$ is the bounce period. Only the sign of $\langle \bar{v}_z \rangle$ matters here, so the in-
 278 tegral in Eq. 6 was evaluated numerically for each particle using the `scipy.integrate.quad`
 279 package in Python 3.8. Particles with positive $\langle \bar{v}_z \rangle$ were categorized into DW+, and the rest
 280 into DW-.

281 **Particle-in-cell simulation** The open-source, fully-relativistic particle-in-cell code,

282 SMILEI[46], was used. The 1D simulation domain was $10\lambda = 100d_i$ long and was divided
 283 into $2^{15} = 32,768$ grid points. Open boundary conditions (Silver-Müller) were employed for
 284 the electromagnetic fields in the x -direction, and periodic boundary conditions were imposed
 285 for the fields in the y -direction and for the particles. 10,000 particles were placed per cell
 286 per species, so about 6×10^8 particles were simulated with a mass ratio $m_i/m_e = 100$. The
 287 simulation run with a frequency ratio of $\omega_{ce}/\omega_{pe} = 5$ is shown in this paper for clarity of
 288 presentation; ratios as low as $\omega_{ce}/\omega_{pe} = 0.2$ were also tried, but lower ratios simply increased
 289 the duration of plasma oscillations that either damp or travel away from the center without
 290 any noticeable effect on the core relaxation mechanism. The initial conditions were Eqs. 1
 291 and 2, and the electrostatic potential $\phi = 0$. The initial temperature was set as one-fifth
 292 of the Harris equilibrium temperature, i.e., $T = 0.2T_{\text{eq}}$ where $T_{\text{eq}} = B_0^2/(4\mu_0 n_0 k_B)$ is the
 293 temperature that yields the Harris equilibrium. The simulation time was $t_{\text{max}} = 100\omega_{ci}^{-1}$
 294 with a time step $\Delta t = 7.63 \times 10^{-4}\omega_{ci}^{-1}$.

295 The simulations were run on the KAIROS computer cluster at Korea Institute of Fusion
 296 Energy.

297 **MMS data and local LMN coordinates** Data from MMS2, MMS3, and MMS4 from
 298 20:24:00 to 20:24:15 UT on June 17, 2017 were averaged to yield the profiles shown in Figs.
 299 5a-e. MMS1 data were omitted because the current density did not exhibit an obvious bi-
 300 furcated structure. The magnetic field data were collected by the Fluxgate Magnetometer
 301 instrument[47] and the plasma data by the Fast Plasma Investigation instrument[48]. The
 302 local LMN coordinate system is obtained from a minimum variance analysis[49] of the aver-
 303 aged raw data which are in Geocentric Solar Ecliptic (GSE) coordinates. The values of the
 304 unit vectors in GSE coordinates are $L = (0.942, 0.308, -0.130)$, $M = (0.194, -0.189, 0.963)$,
 305 and $N = (0.272, -0.932, -0.238)$ in GSE coordinates. L is the direction of the sheared mag-
 306 netic field, N is the direction normal to the current sheet, and LMN form a right-handed
 307 coordinate system.

308 DATA AVAILABILITY

309 MMS data are publicly available from <https://lasp.colorado.edu/mms/sdc/public>. The
 310 data from the PIC simulations are available from <https://doi.org/10.5281/zenodo.4607112>.

311 **CODE AVAILABILITY**

312 SMILEI[46] is an open-source PIC code available from <https://smileipic.github.io/Smilei>.

313 MMS data were analyzed using the pySPEDAS package, available from <https://github.com/spedas/pyspedas>

314 The codes used in the data analyses are available from Y.D.Y. upon reasonable request.

-
- 315 [1] Linhui Sui and Gordon D. Holman. Evidence for the Formation of a Large-Scale Current Sheet
316 in a Solar Flare. *The Astrophysical Journal*, 596(2):L251–L254, oct 2003.
- 317 [2] Steven J. Schwartz, Chris P. Chaloner, Peter J. Christiansen, Andrew J. Coates, David S.
318 Hall, Alan D. Johnstone, M. Paul Gough, Andrew J. Norris, Richard P. Rijnbeek, David J.
319 Southwood, and Les J.C. Woolliscroft. An active current sheet in the solar wind. *Nature*,
320 318(6043):269–271, nov 1985.
- 321 [3] J. Todd Hoeksema, John M. Wilcox, and Philip H. Scherrer. Structure of the Heliospheric
322 Current Sheet: 1978-1982. *Journal of Geophysical Research*, 88(A12):9910–9918, 1983.
- 323 [4] Edward J. Smith. The heliospheric current sheet. *Journal of Geophysical Research: Space*
324 *Physics*, 106(A8):15819–15831, aug 2001.
- 325 [5] T. W. Speiser. Magnetospheric current sheets. *Radio Science*, 8(11):973–977, nov 1973.
- 326 [6] Krishan K. Khurana and Hannes K. Schwarzl. Global structure of Jupiter’s magnetospheric
327 current sheet. *Journal of Geophysical Research: Space Physics*, 110(A7):A07227, 2005.
- 328 [7] Masaaki Yamada, Hantao Ji, Scott Hsu, Troy Carter, Russell Kulsrud, and Fedor Trintchouk.
329 Experimental investigation of the neutral sheet profile during magnetic reconnection. *Physics*
330 *of Plasmas*, 7(5):1781–1787, may 2000.
- 331 [8] Masaaki Yamada, Russell Kulsrud, and Hantao Ji. Magnetic reconnection. *Reviews of Modern*
332 *Physics*, 82(1):603–664, mar 2010.
- 333 [9] E. G. Harris. On a plasma sheath separating regions of oppositely directed magnetic field. *Il*
334 *Nuovo Cimento*, 23(1):115–121, jan 1962.
- 335 [10] J. R. Kan. On the structure of the magnetotail current sheet. *Journal of Geophysical Research*,
336 78(19):3773–3781, jul 1973.
- 337 [11] Paul J. Channell. Exact Vlasov-Maxwell equilibria with sheared magnetic fields. *Physics of*
338 *Fluids*, 19(10):1541–1545, 1976.

- 339 [12] B. Lembège and R. Pellat. Stability of a thick two-dimensional quasineutral sheet. *Physics of*
340 *Fluids*, 25(11):1995, 1982.
- 341 [13] A P Kropotkin, H V Malova, and M I Sitnov. Self-consistent structure of a thin anisotropic
342 current sheet. *Journal of Geophysical Research: Space Physics*, 102(A10):22099–22106, oct
343 1997.
- 344 [14] Peter H. Yoon, Anthony T. Y. Lui, and Robert B. Sheldon. On the current sheet model with
345 κ distribution. *Physics of Plasmas*, 13(10):102108, oct 2006.
- 346 [15] Michael G. Harrison and Thomas Neukirch. One-Dimensional Vlasov-Maxwell Equilibrium for
347 the Force-Free Harris Sheet. *Physical Review Letters*, 102(13):135003, apr 2009.
- 348 [16] L. M. Zelenyi, H. V. Malova, A. V. Artemyev, V. Yu Popov, and A. A. Petrukovich. Thin
349 current sheets in collisionless plasma: Equilibrium structure, plasma instabilities, and particle
350 acceleration. *Plasma Physics Reports*, 37(2):118–160, feb 2011.
- 351 [17] J.W. Eastwood. Consistency of fields and particle motion in the 'Speiser' model of the current
352 sheet. *Planetary and Space Science*, 20(10):1555–1568, oct 1972.
- 353 [18] P. L. Pritchett and F. V. Coroniti. Formation and stability of the self-consistent one-
354 dimensional tail current sheet. *Journal of Geophysical Research*, 97(A11):16773, nov 1992.
- 355 [19] G. R. Burkhart, J. F. Drake, P. B. Dusenbery, and T. W. Speiser. A particle model for
356 magnetotail neutral sheet equilibria. *Journal of Geophysical Research*, 97(A9):13799, 1992.
- 357 [20] Luxiuyuan Jiang and San Lu. Externally driven bifurcation of current sheet: A particle-in-cell
358 simulation. *AIP Advances*, 11(1):015001, jan 2021.
- 359 [21] A. Runov, R. Nakamura, W. Baumjohann, T. L. Zhang, M. Volwerk, H.-U. Eichelberger, and
360 A. Balogh. Cluster observation of a bifurcated current sheet. *Geophysical Research Letters*,
361 30(2):3–6, jan 2003.
- 362 [22] A. Runov, R. Nakamura, W. Baumjohann, R. A. Treumann, T. L. Zhang, and M. Volw-
363 erk. Current sheet structure near magnetic X-line observed by Cluster. *Geophysical Research*
364 *Letters*, 30(11):1579, 2003.
- 365 [23] Yoshihiro Asano. How typical are atypical current sheets? *Geophysical Research Letters*,
366 32(3):L03108, 2005.
- 367 [24] S. M. Thompson, M. G. Kivelson, M. El-Alaoui, A. Balogh, H. Réme, and L. M. Kistler.
368 Bifurcated current sheets: Statistics from Cluster magnetometer measurements. *Journal of*
369 *Geophysical Research*, 111(A3):A03212, 2006.

- 370 [25] V. Sergeev, A. Runov, W. Baumjohann, R. Nakamura, T. L. Zhang, M. Volwerk, A. Balogh,
371 H. Rème, J. A. Sauvaud, M. André, and B. Klecker. Current sheet flapping motion and
372 structure observed by Cluster. *Geophysical Research Letters*, 30(6):2–5, mar 2003.
- 373 [26] M. Hoshino, A. Nishida, T. Mukai, Y. Saito, T. Yamamoto, and S. Kokubun. Structure of
374 plasma sheet in magnetotail: Double-peaked electric current sheet. *Journal of Geophysical*
375 *Research: Space Physics*, 101(A11):24775–24786, nov 1996.
- 376 [27] Y. Asano, T. Mukai, M. Hoshino, Y. Saito, H. Hayakawa, and T. Nagai. Current sheet
377 structure around the near-Earth neutral line observed by Geotail. *Journal of Geophysical*
378 *Research: Space Physics*, 109(A2):1–18, feb 2004.
- 379 [28] M. I. Sitnov, P. N. Guzdar, and M. Swisdak. A model of the bifurcated current sheet. *Geo-*
380 *physical Research Letters*, 30(13):10–13, jul 2003.
- 381 [29] L. M. Zelenyi, H. V. Malova, V. Yu Popov, D. Delcourt, and A. S. Sharma. Nonlinear equi-
382 librium structure of thin currents sheets: influence of electron pressure anisotropy. *Nonlinear*
383 *Processes in Geophysics*, 11(5/6):579–587, nov 2004.
- 384 [30] Don E George and Jörg-Micha Jahn. Energized Oxygen in the Magnetotail: Current
385 Sheet Bifurcation From Speiser Motion. *Journal of Geophysical Research: Space Physics*,
386 125(2):e2019JA027339, feb 2020.
- 387 [31] J. L. Burch and T. D. Phan. Magnetic reconnection at the dayside magnetopause: Advances
388 with MMS. *Geophysical Research Letters*, 43(16):8327–8338, aug 2016.
- 389 [32] M. Zhou, H. Y. Man, Z. H. Zhong, X. H. Deng, Y. Pang, S. Y. Huang, Y. Khotyaintsev, C. T.
390 Russell, and B. Giles. Sub-ion-scale Dynamics of the Ion Diffusion Region in the Magnetotail:
391 MMS Observations. *Journal of Geophysical Research: Space Physics*, 124(10):7898–7911, oct
392 2019.
- 393 [33] Rongsheng Wang, Quanming Lu, San Lu, Christopher T. Russell, J. L. Burch, Daniel J.
394 Gershman, W. Gonzalez, and Shui Wang. Physical Implication of Two Types of Reconnection
395 Electron Diffusion Regions With and Without Ion-Coupling in the Magnetotail Current Sheet.
396 *Geophysical Research Letters*, 47(21):e2020GL088761, nov 2020.
- 397 [34] B. U. Ö. Sonnerup. Adiabatic particle orbits in a magnetic null sheet. *Journal of Geophysical*
398 *Research*, 76(34):8211–8222, dec 1971.
- 399 [35] T. W. Speiser. Particle trajectories in model current sheets: 1. Analytical solutions. *Journal*
400 *of Geophysical Research*, 70(17):4219–4226, sep 1965.

- 401 [36] Jörg Büchner and Lev M. Zelenyi. Regular and chaotic charged particle motion in magneto-
402 taillike field reversals: 1. Basic theory of trapped motion. *Journal of Geophysical Research*,
403 94(A9):11821, 1989.
- 404 [37] L. M. Zelenyi, H. V. Malova, and V. Yu Popov. Splitting of thin current sheets in the Earth’s
405 magnetosphere. *Journal of Experimental and Theoretical Physics Letters*, 78(5):296–299, sep
406 2003.
- 407 [38] John R Cary, D F Escande, and J L Tennyson. Adiabatic-invariant change due to separatrix
408 crossing. *Physical Review A*, 34(5):4256–4275, nov 1986.
- 409 [39] J. L. Burch, T. E. Moore, R. B. Torbert, and B. L. Giles. Magnetospheric Multiscale Overview
410 and Science Objectives. *Space Science Reviews*, 199(1-4):5–21, mar 2016.
- 411 [40] Rongsheng Wang, Quanming Lu, Rumi Nakamura, Wolfgang Baumjohann, Can Huang,
412 Christopher T. Russell, J. L. Burch, Craig J. Pollock, Dan Gershman, R. E. Ergun, Shui
413 Wang, P. A. Lindqvist, and Barbara Giles. An Electron-Scale Current Sheet Without Bursty
414 Reconnection Signatures Observed in the Near-Earth Tail. *Geophysical Research Letters*,
415 45(10):4542–4549, may 2018.
- 416 [41] San Lu, Rongsheng Wang, Quanming Lu, V. Angelopoulos, R. Nakamura, A. V. Artemyev,
417 P. L. Pritchett, T. Z. Liu, X.-J. Zhang, W. Baumjohann, W. Gonzalez, A. C. Rager, R. B.
418 Torbert, B. L. Giles, D. J. Gershman, C. T. Russell, R. J. Strangeway, Y. Qi, R. E. Ergun, P.-
419 A. Lindqvist, J. L. Burch, and Shui Wang. Magnetotail reconnection onset caused by electron
420 kinetics with a strong external driver. *Nature Communications*, 11(1):5049, dec 2020.
- 421 [42] M. A. Shay, C. C. Haggerty, T. D. Phan, J. F. Drake, P. A. Cassak, P. Wu, M. Oieroset,
422 M. Swisdak, and K. Malakit. Electron heating during magnetic reconnection: A simulation
423 scaling study. *Physics of Plasmas*, 21(12), 2014.
- 424 [43] J. T. Gosling and A. Szabo. Bifurcated current sheets produced by magnetic reconnection in
425 the solar wind. *Journal of Geophysical Research: Space Physics*, 113(A10):1–8, oct 2008.
- 426 [44] Y. Asano, T. Mukai, M. Hoshino, Y. Saito, H. Hayakawa, and T. Nagai. Evolution of the
427 thin current sheet in a substorm observed by Geotail. *Journal of Geophysical Research: Space
428 Physics*, 108(A5):1–10, may 2003.
- 429 [45] J. Birn, J. F. Drake, M. A. Shay, B. N. Rogers, R. E. Denton, M. Hesse, M. Kuznetsova,
430 Z. W. Ma, A. Bhattacharjee, A. Otto, and P. L. Pritchett. Geospace Environmental Modeling
431 (GEM) Magnetic Reconnection Challenge. *Journal of Geophysical Research: Space Physics*,

- 432 106(A3):3715–3719, mar 2001.
- 433 [46] J. Derouillat, A. Beck, F. Pérez, T. Vinci, M. Chiaramello, A. Grassi, M. Flé, G. Bouchard,
434 I. Plotnikov, N. Aunai, J. Dargent, C. Riconda, and M. Grech. SMILEI: A collaborative, open-
435 source, multi-purpose particle-in-cell code for plasma simulation. *Computer Physics Commu-
436 nications*, 222:351–373, jan 2018.
- 437 [47] R. B. Torbert, C. T. Russell, W. Magnes, R. E. Ergun, P.-A. Lindqvist, O. LeContel, H. Vaith,
438 J. Macri, S. Myers, D. Rau, J. Needell, B. King, M. Granoff, M. Chutter, I. Dors, G. Olsson,
439 Y. V. Khotyaintsev, A. Eriksson, C. A. Kletzing, S. Bounds, B. Anderson, W. Baumjohann,
440 M. Steller, K. Bromund, Guan Le, R. Nakamura, R. J. Strangeway, H. K. Leinweber, S. Tucker,
441 J. Westfall, D. Fischer, F. Plaschke, J. Porter, and K. Lappalainen. The FIELDS Instrument
442 Suite on MMS: Scientific Objectives, Measurements, and Data Products. *Space Science Re-
443 views*, 199(1-4):105–135, mar 2016.
- 444 [48] C. Pollock, T. Moore, A. Jacques, J. Burch, U. Gliese, Y. Saito, T. Omoto, L. Avanov, A. Bar-
445 rie, V. Coffey, J. Dorelli, D. Gershman, B. Giles, T. Rosnack, C. Salo, S. Yokota, M. Adrian,
446 C. Aoustin, C. Auletta, S. Aung, V. Bigio, N. Cao, M. Chandler, D. Chornay, K. Chris-
447 tian, G. Clark, G. Collinson, T. Corris, A. De Los Santos, R. Devlin, T. Diaz, T. Dickerson,
448 C. Dickson, A. Diekmann, F. Diggs, C. Duncan, A. Figueroa-Vinas, C. Firman, M. Free-
449 man, N. Galassi, K. Garcia, G. Goodhart, D. Guererro, J. Hageman, J. Hanley, E. Hem-
450 minger, M. Holland, M. Hutchins, T. James, W. Jones, S. Kreisler, J. Kujawski, V. Lavu,
451 J. Lobell, E. LeCompte, A. Lukemire, E. MacDonald, A. Mariano, T. Mukai, K. Narayanan,
452 Q. Nguyen, M. Onizuka, W. Paterson, S. Persyn, B. Piepgrass, F. Cheney, A. Rager, T. Raghu-
453 ram, A. Ramil, L. Reichenthal, H. Rodriguez, J. Rouzaud, A. Rucker, Y. Saito, M. Samara,
454 J.-A. Sauvaud, D. Schuster, M. Shappirio, K. Shelton, D. Sher, D. Smith, K. Smith, S. Smith,
455 D. Steinfeld, R. Szymkiewicz, K. Tanimoto, J. Taylor, C. Tucker, K. Tull, A. Uhl, J. Vloet,
456 P. Walpole, S. Weidner, D. White, G. Winkert, P.-S. Yeh, and M. Zeuch. Fast Plasma Inves-
457 tigation for Magnetospheric Multiscale. *Space Science Reviews*, 199(1-4):331–406, mar 2016.
- 458 [49] Buo Sonnerup and Maureen Scheible. Minimum and maximum variance analysis. In *Analysis
459 methods for multi-spacecraft data*, volume 001, pages 185–220. 1998.

460 **ACKNOWLEDGMENTS**

461 This work was supported by the National Research Foundation of Korea under grant
462 nos. NRF-2019R1C1C1003412, NRF-2019R1A2C1004862, and 2019M1A7A1A03088456.
463 We thank the entire MMS team and MMS Science Data Center for providing the high-
464 quality data for this study. We also thank J. M. Kwon, J. H. Kim, and Korea Institute of
465 Fusion Energy for providing the computer resources.

466 **AUTHOR CONTRIBUTIONS**

467 Y.D.Y. conceived the central idea, performed the simulations and theoretical analysis,
468 analyzed the spacecraft data, and wrote the manuscript based on extensive discussions with
469 G.S.Y. D.E.W. contributed to the interpretation of the simulation and observation results,
470 as well as to the revision of the draft. J.L.B. oversaw the MMS project and provided general
471 guidance.

472 **Correspondence** and requests for materials should be addressed to Y.D.Y or G.S.Y.

473 **COMPETING INTERESTS**

474 The authors declare no competing interests.

Figures

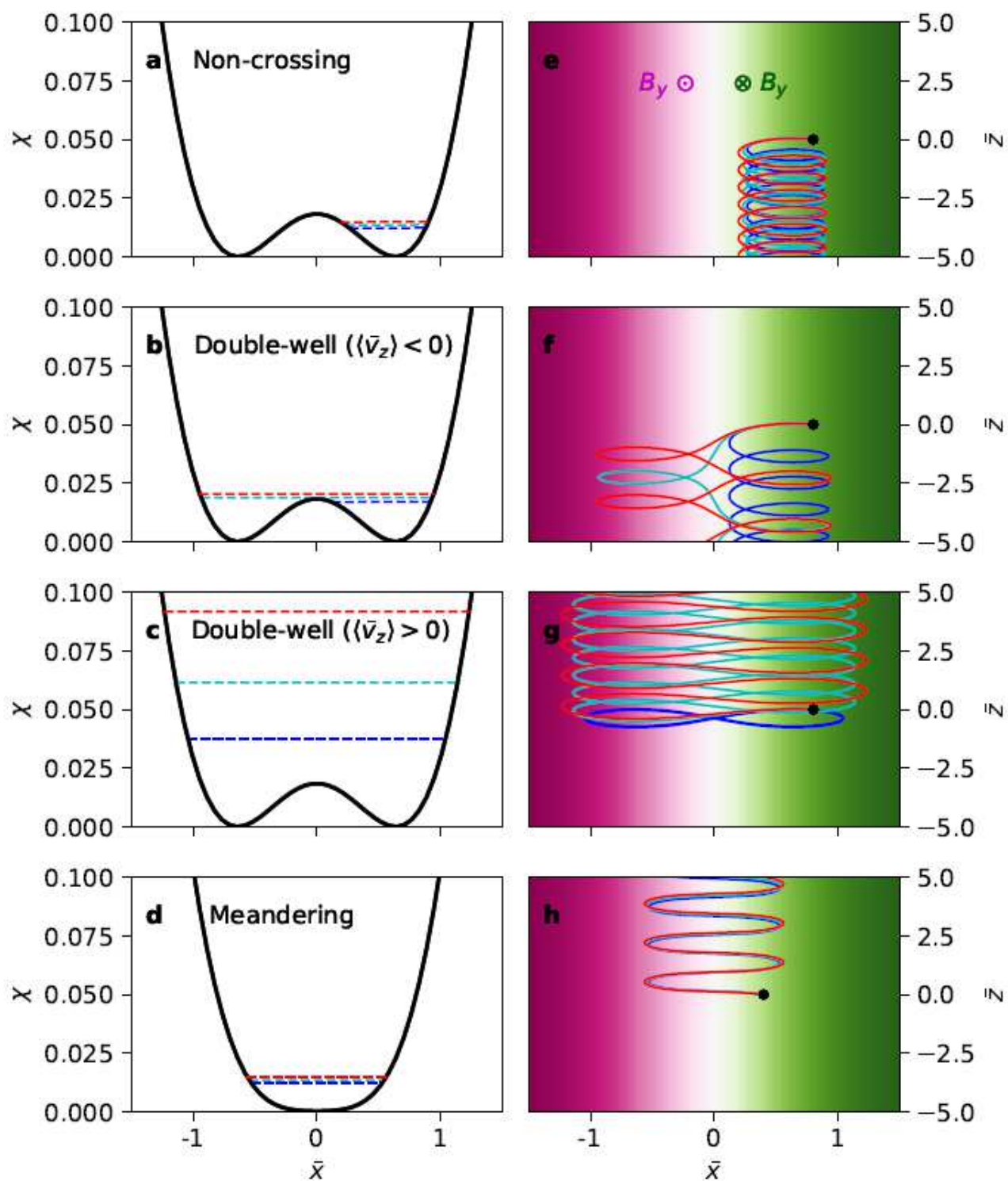


Figure 1

Four classes of particle orbits and their effective potentials. Please see manuscript .pdf for full caption.

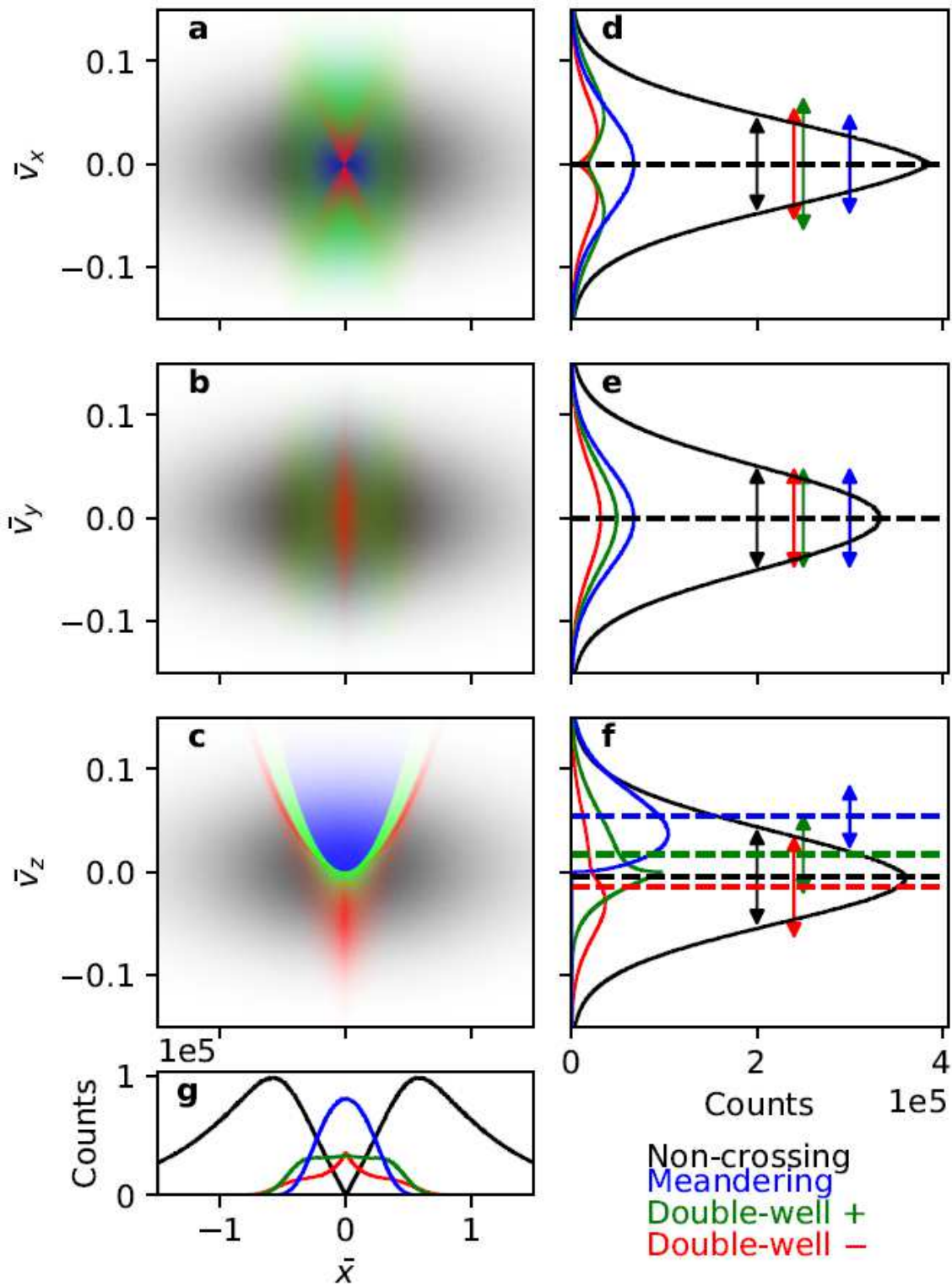


Figure 2

Particle distribution in phase space, velocity space, and physical space. Please see manuscript .pdf for full caption.

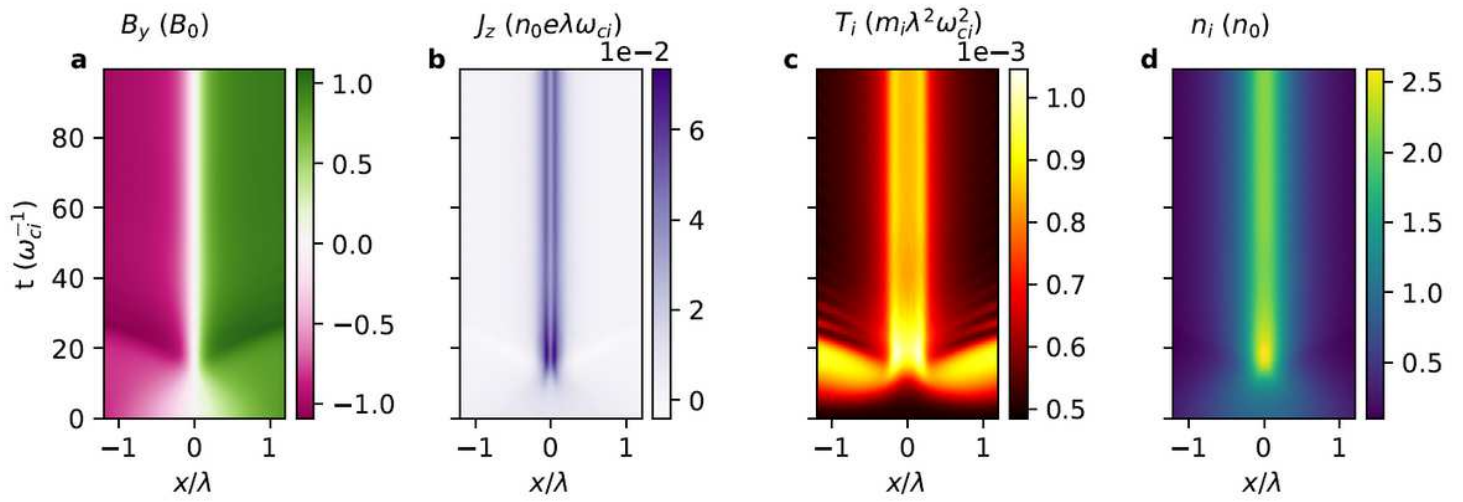


Figure 3

Streak plots of variables from the particle-in-cell simulation. Please see manuscript .pdf for full caption.

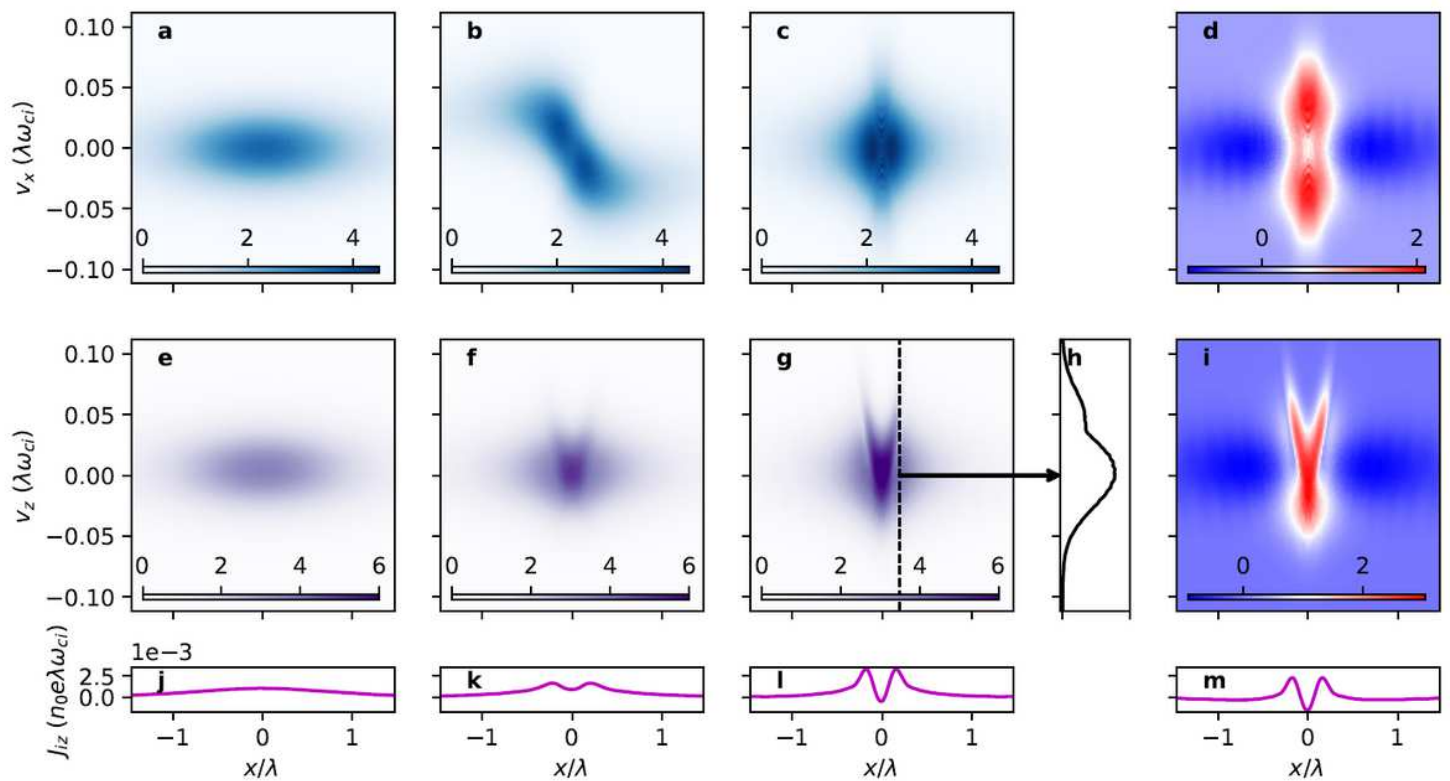


Figure 4

Time evolution of the ion distribution function from the particle-in-cell simulation. Please see manuscript .pdf for full caption.

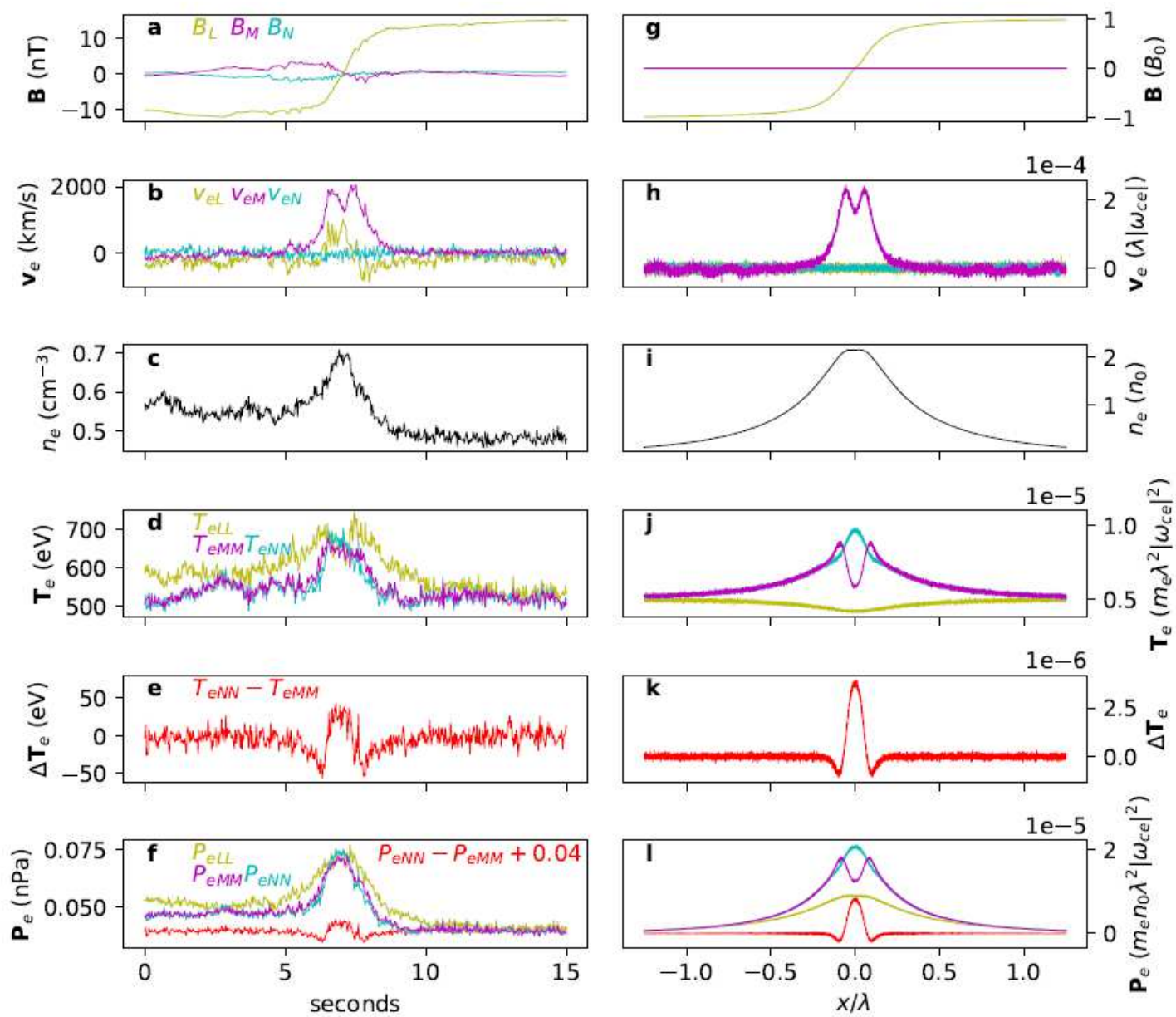


Figure 5

Comparison of a current sheet detected by MMS to that from the particle-in-cell simulation. Please see manuscript .pdf for full caption.